The divergence-free velocity formulation of the consistent Navier-Stokes Cahn-Hilliard model with non-matching densities, divergence-conforming discretization, and benchmarks

M.F.P. ten Eikelder*, D. Schillinger

Institute for Mechanics, Computational Mechanics Group, Technische Universität Darmstadt, Franziska-Braun-Str. 7, 64287 Darmstadt, Germany

Abstract

The prototypical diffuse-interface model that describes multi-component flows is the Navier-Stokes Cahn-Hilliard model (NSCH). Over the last decades many NSCH models have appeared that claim to describe the same physical phenomena, yet are distinct from one another. In a recent article [M.F.P. ten Eikelder, K.G. van der Zee, I. Akkerman, and D. Schillinger, Math. Mod. Meth. Appl. S. 33, pp 175-221, 2023.] we have established a unified framework of virtually all NSCH models. The framework reveals that there is only a single consistent NSCH model that naturally emanates from the underlying mixture theory. In the current article we present, verify and validate this novel consistent NSCH model by means of numerical simulation. To this purpose we discretize a divergence-free velocity formulation of the NSCH model using divergence-conforming isogeometric spaces. We compare computations of our consistent model to results of existing models from literature. The predictive capability of the numerical methodology is demonstrated via three-dimensional computations of a rising bubble and the contraction of a liquid filament that compare well with experimental data.

Keywords: Navier-Stokes Cahn-Hilliard model, Non-matching densities, Divergence-conforming simulation, Isogeometric analysis, Rising bubbles, Ligament contraction

1. Introduction

The Navier-Stokes Cahn-Hilliard (NSCH) model is a diffuse-interface flow model that describes the evolution of viscous incompressible isothermal fluid mixtures. This model has proven to be powerful approach for the simulation of free-surface problems in which topological changes, surface tension, and density jumps play an important role. Typical examples of these problems include the deformation, coalescence or break-up of bubble or droplets.

The development of NSCH models started with matching density models proposed by Hohenberg and Halperin [1] and Gurtin [2]. Over the last decades, the design of Navier-Stokes Cahn-Hilliard models has been extended to the non-matching density case with important contributions by Lowengrub and Truskinovsky [3], Boyer [4], Ding et al. [5], Abels et al. [6], Shen et al. [7], Aki et al. [8] and Shokrpour Roudbari et al. [9]. Each of these works aims to describe the same physics, yet the proposed models are different. In particular, three problems occur: (1) the systems of balance laws of the various models are distinct before constitutive choices have been applied, (2) the energy-dissipation laws of the models are conflicting, and (3) some of the models are inconsistent in the single fluid regime. As such, there is no consensus in the realm of NSCH models, and the connection between the existing NSCH models has been mostly unexplored.

---

*Corresponding author

Email addresses: `marco.ten-eikelder@tu-darmstadt.de` (M.F.P. ten Eikelder), `dominik.schillinger@tu-darmstadt.de` (D. Schillinger)

In our recent article [10] we have revealed the sought-after connections by establishing a unified framework of NSCH models with non-matching densities[1]. Given that each of the models aims to describe the same physics, it is only natural to anticipate a *single NSCH model*, not a collection of models. Of course, variations appear in the selection of constitutive models, but the general (form of the) model is fixed. Indeed, the unified framework naturally leads to a single NSCH model. This model is invariant to the set of fundamental variables. After applying small but important corrections, and subsequently applying simple variable transformations, the connection to virtually all existing NSCH models is established. For example, the longstanding belief is that there are two distinct classes of models, (i) models with mass-averaged velocities and (ii) models with volume-averaged velocities. Our framework indicates that these seemingly different classes of models are in fact two sides of the same coin; simple variable transformations reveal that these classes of models are equivalent.

Since the NSCH models describe the flow equations of a mixture of fluids, the correct theoretical framework is *continuum mixture theory*, as proposed by Truesdell and Toupin [11, 12]. It appears that existing NSCH models are only partly established via mixture theory. As a consequence, either the balance laws are not compatible with mixture theory before constitutive modeling, or the final model is inconsistent in the single fluid regime. As such, none of the NSCH models in literature is fully compatible with the NSCH model, see Table 1, and (small) rectifications are necessary to match the *consistent* NSCH model that we have introduced in [10]. The term *consistent* conveys that the NSCH model is established in a consistent manner through mixture theory. Hence, the balance laws naturally emerge from mixture theory, and the model matches the incompressible Navier-Stokes equations in the single fluid regime.

Model	MT-consistent BL	Single fluid	Energy-dissipation
Abels et al. [6]	✗	✓	★
Aki et al. [8]	✓	✗	✓
Boyer [4]	✗	✓	✗
Ding et al. [5]	✗	✓	✗
Lowengrub and Truskinovsky [3]	✓	✗	✓
Shen et al. [7]	✓	✗	✓
Shokrpour Roudbari et al. [9]	✓	✗	✓
Consistent NSCH model [10]	✓	✓	✓

Table 1: Comparison of the various NSCH models. The column 'MT-consistent BL' indicates whether the balance laws (BL) of the model are compatible with mixture theory (MT). In the third column 'Single fluid' we state whether the model is compatible with the incompressible Navier-Stokes equation in the single fluid regime, and in the last column whether the model is energy dissipative. The symbol ★ indicates that there exists an energy-dissipation law in which the associated kinetic energy is not an obvious approximation of the kinetic energy of the mixture. We refer to ten Eikelder et al. [10] for details.

We refer from now on to *the NSCH model*, of which a particular form reads:

$$\partial_t(\rho\mathbf{v}) + \mathrm{div}\,(\rho\mathbf{v} \otimes \mathbf{v}) + \nabla p + \phi\nabla\mu - \mathrm{div}\,\boldsymbol{\tau} - \rho\mathbf{g} = 0, \tag{1a}$$

$$\partial_t\rho + \mathrm{div}(\rho\mathbf{v}) = 0, \tag{1b}$$

$$\partial_t\phi + \mathrm{div}(\phi\mathbf{v}) - \mathrm{div}\,(\mathbf{M}^v\nabla\,(\mu + \alpha p)) = 0, \tag{1c}$$

$$\mu - \frac{\partial\Psi}{\partial\phi} + \mathrm{div}\left(\frac{\partial\Psi}{\partial\nabla\phi}\right) = 0, \tag{1d}$$

---

[1]This framework encompasses mass transfer between constituents resulting in models of Navier-Stokes Cahn-Hilliard Allen-Cahn type. In the current work we assume the absence of constituent mass transfer, and thus deal with Navier-Stokes Cahn-Hilliard models.

in domain $\Omega \subset \mathbb{R}^d$. Here $\mathbf{v}$ is the mass averaged velocity, ρ the mixture density, ν the dynamic viscosity, p the mechanical pressure and ϕ the phase variable. Furthermore μ is a chemical potential quantity, $W = W(\phi)$ a double-well potential, Ψ the volumetric free energy, $\mathbf{M}^v$ a degenerate mobility tensor, $\boldsymbol{g}$ a force vector, α a constant linked to the density jump, and $\boldsymbol{\tau}$ is the Cauchy stress. The constant surface tension coefficient is σ and ϵ is a parameter associated with the interface thickness. We remark that the reference of this model as a Cahn-Hilliard type model originates from the fact that (1c) is a (convective) Cahn-Hilliard equation when selecting the Ginzburg-Landau free energy for Ψ.

We emphasize that the NSCH model is a reduced model from the perspective of continuum mixture theory. Namely, the NSCH model consists of a single momentum equation, whereas a full mixture model would contain one momentum equation per constituent. We have recently established a diffuse-interface modeling framework [13] that is fully compatible with mixture theory. This model does not contain any Cahn-Hilliard type equation (and thus no associated mobility parameter), however the Allen-Cahn mass transfer model remains present. This accentuates that the Cahn-Hilliard component in the NSCH model emerges from a simplication assumption of NSCH model which does not match with mixture theory.

Over the last decades a large number of numerical methods has been presented for NSCH models with non-matching densities, see e.g. [4, 5, 7, 9, 14–16]. It is well-known in the community that it is hard (or perhaps impossible) to monolitlically discretize a mass-averaged velocity form of the NSCH model. In fact, the authors are not aware of any such numerical methodology. As a consequence, the volume-averaged velocity form of the NSCH model is more popular in the design of numerical methods. This is due to the fact that (in absense of mass transfer) this velocity is divergence-free and one can adopt standard stable velocity/pressure finite element pairs.

In this current article we present the consistent NSCH model along with its first numerical discretization, a verification study, and a validation with experimental data. To this purpose, we transform (1) into an equivalent formulation in terms of a divergence-free velocity. This circumvents the numerical difficulty of the mass-averaged velocity form of the model (1). We then propose a monolithic discretization methodology that makes use of divergence conforming isogeometric analysis spaces. We note that the usage of these spaces for the discretization of a NSCH model is uncommon but not new, see Espath et al. [17]. Finally, we perform a two-dimensional verification, and a three-dimensional validation study.

The remainder of the paper is outlined as follows. In Section 2 we present the consistent Navier-Stokes Cahn-Hilliard model and analyze its properties. Additionally, we present an alternative but equivalent formulation that forms the basis for the discretization scheme. In Section 3 we introduce the fully-discrete numerical scheme and its properties. Next, in Section 4 we compare the proposed method to computations of existing models from literature. Then, in Section 5 we simulate a number of three-dimensional benchmark problems. We close the paper with a conclusion and outlook in Section 6.

2. The Navier-Stokes Cahn-Hilliard model

In this section we present the consistent Navier-Stokes Cahn-Hilliard model. First, in Section 2.1 we present the governing equations, and select compatible constitutive models. Then, in Section 2.2 we discuss the physical properties of the model. In Section 2.3 we perform the non-dimensionalization.

2.1. Governing equations and divergence-free formulation

The derivation of the consistent Navier-Stokes Cahn-Hilliard model relies on mixture theory and the Coleman-Noll procedure. A detailed derivation and discussion on the various modeling choices can be found in ten Eikelder et al. [10]. In this article we work with the NSCH initial/boundary value problem (1) which we repeat in detail: find the mass-averaged velocity $\mathbf{v} : \Omega \to \mathbb{R}^d$, the pressure $p : \Omega \to \mathbb{R}$, the phase field

3

$\phi : \Omega \to [-1, 1]$ and the chemical potential $\mu : \Omega \to \mathbb{R}$ such that:

$$\partial_t(\rho\mathbf{v}) + \text{div}(\rho\mathbf{v} \otimes \mathbf{v}) + \nabla p + \phi\nabla\mu - \text{div}\boldsymbol{\tau} - \rho\mathbf{g} = 0, \tag{2a}$$

$$\partial_t\rho + \text{div}(\rho\mathbf{v}) = 0, \tag{2b}$$

$$\partial_t\phi + \text{div}(\phi\mathbf{v}) - \text{div}\left(\mathbf{M}^v\nabla(\mu + \alpha p)\right) = 0, \tag{2c}$$

$$\mu - \frac{\partial\Psi}{\partial\phi} + \text{div}\left(\frac{\partial\Psi}{\partial\nabla\phi}\right) = 0. \tag{2d}$$

with $\mathbf{v}(\mathbf{x}, 0) = \mathbf{v}_0(\mathbf{x})$ and $\phi(\mathbf{x}, 0) = \phi_0(\mathbf{x})$ in Ω. The phase variable ϕ represents the difference of the volume fractions of the two constituents; $\phi = 1$ in the first constituent whereas $\phi = -1$ in the second constituent. The density ρ and the dynamic viscosity ν are the superposition of the constant constituent quantities (ρ_1, ρ_2 and ν_1, ν_2) weighted by their volume fractions:

$$\rho(\phi) = \rho_1\frac{1+\phi}{2} + \rho_2\frac{1-\phi}{2},$$

$$\nu(\phi) = \nu_1\frac{1+\phi}{2} + \nu_2\frac{1-\phi}{2}, \tag{3a}$$

with constant constituent densities ρ_1 and ρ_2 and constant constituent viscosities ν_1 and ν_2. Furthermore, $\mathbf{g} = -g\boldsymbol{\jmath}$, where $\boldsymbol{\jmath}$ is the vertical unit vector and g the gravitational acceleration, and $\alpha = (\rho_2 - \rho_1)/(\rho_1 + \rho_2)$ is a constant linked to the relative density jump. The Cauchy stress is of the form $\boldsymbol{\tau} = \nu(2\mathbf{D} + \lambda(\text{div}\mathbf{v})\mathbf{I})$ where $\mathbf{D} = (\nabla\mathbf{v} + (\nabla\mathbf{v})^T)/2$ is the symmetric velocity gradient, and the factor $\lambda\nu$ represents the second viscosity coefficient. In this work we assume that the Stokes's hypothesis is fulfilled, i.e. $\lambda = -2/d$, where d is the number of spatial dimensions. Next, Ψ denotes the Helmholtz free energy functional belonging to the constitutive class:

$$\Psi = \Psi(\phi, \nabla\phi). \tag{4}$$

The quantity μ represents a chemical potential-like variable and is defined as the variational derivative of the integral of the Helmholtz free energy Ψ, i.e.:

$$\mu := \frac{\partial\Psi}{\partial\phi} - \text{div}\frac{\partial\Psi}{\partial\nabla\phi}. \tag{5}$$

The so-called mobility tensor $\mathbf{M}^v = \mathbf{M}^v(\phi, \nabla\phi, \mu, \nabla\mu, p)$ is a scaling factor of the term $\nabla(\mu + \alpha p)$. This product is a model for velocity difference of the two components, see [10]. The mobility tensor is of degenerate type. This means that in the single-fluid regime, i.e. $\phi = \pm 1$, the mobility vanishes: $\mathbf{M}^v = 0$. Furthermore, $\mathbf{M}^v$ is compatible with the condition:

$$-\nabla(\mu + \alpha p) \cdot \mathbf{M}^v\nabla(\mu + \alpha p) \leq 0. \tag{6}$$

Equation (2a) represents the balance of mixture momentum, and (2b) the balance of mixture mass. Next, (2c) is the phase field equation, that due to the degenerate type of the mobility tensor, is compatible in the single fluid regime. Lastly, equation defines the variational derivative of the free energy and may be substituted into (2a) and (2c).

We now convert the form (2) of the NSCH model by means of the variable transformation:

$$\rho\mathbf{v} = \rho\mathbf{u} + \mathbf{J}, \tag{7}$$

where the diffusive flux $\mathbf{J} = \mathbf{J}(p, \phi, \mu)$, and the degenerate mobility tensor $\mathbf{M}$ are given by:

$$\mathbf{J} = -\frac{\rho_1 - \rho_2}{2}\mathbf{M}\nabla(\mu + \alpha p), \tag{8a}$$

$$\mathbf{M} = \left(2\rho/\left(\rho_1 + \rho_2\right)\right)\mathbf{M}^v. \tag{8b}$$

The (equivalent) NSCH initial/boundary value problem now takes the form: find the volume-averaged velocity $\mathbf{u} : \Omega \to \mathbb{R}^d$, the pressure $p : \Omega \to \mathbb{R}$, the phase field $\phi : \Omega \to [-1, 1]$ and the chemical potential $\mu : \Omega \to \mathbb{R}$ such that:

$$\partial_t(\rho\mathbf{u} + \mathbf{J}) + \mathrm{div}\left(\rho^{-1}\left(\rho\mathbf{u} + \mathbf{J}\right) \otimes \left(\rho\mathbf{u} + \mathbf{J}\right)\right) + \nabla p + \phi\nabla\mu - \mathrm{div}\boldsymbol{\tau} - \rho\mathbf{g} = 0, \tag{9a}$$

$$\mathrm{div}\mathbf{u} = 0, \tag{9b}$$

$$\partial_t\phi + \mathbf{u} \cdot \nabla\phi - \mathrm{div}\left(\mathbf{M}\nabla\left(\mu + \alpha p\right)\right) = 0, \tag{9c}$$

$$\mu - \frac{\partial\Psi}{\partial\phi} + \mathrm{div}\left(\frac{\partial\Psi}{\partial\nabla\phi}\right) = 0, \tag{9d}$$

with $\mathbf{u}(\mathbf{x}, 0) = \mathbf{u}_0(\mathbf{x})$, $\phi(\mathbf{x}, 0) = \phi_0(\mathbf{x})$ and $p(\mathbf{x}, 0) = p_0(\mathbf{x})$ in Ω. The Cauchy stress $\boldsymbol{\tau} = \boldsymbol{\tau}(\mathbf{u}, p, \phi, \mu)$ and symmetric velocity gradient $\mathbf{D}$ take the form:

$$\boldsymbol{\tau} = \nu\left(2\mathbf{D} + \lambda\mathrm{div}\left(\rho^{-1}\mathbf{J}\right)\mathbf{I}\right), \tag{10a}$$

$$\mathbf{D} = \nabla\left(\mathbf{u} + \rho^{-1}\mathbf{J}\right)/2 + \nabla\left(\mathbf{u} + \rho^{-1}\mathbf{J}\right)^T/2, \tag{10b}$$

The balance of mixture momentum (9a) is non-standard due to the form of the inertia terms. The mixture momentum equation of existing volume-averaged velocity models is incomplete when compared with (9a). Namely, these existing models either do not accommodate any diffusive flux ($\mathbf{J}$) [4, 5], or contain just a single diffusive flux [6]. The occurrence of the diffusive flux $\mathbf{J}$ in the mixture momentum equation is not new. Next, (9b) represents the divergence free property of the velocity field. This key structure of the formulation coincides with the single-fluid incompressible Navier-Stokes equations. Finally, (9c) is the phase field equation, and (9d) defines the variational derivative of the free energy.

In this paper we work with the Helmholtz free energy in the Ginzburg-Landau form:

$$\Psi = \frac{\sigma}{\varepsilon}W(\phi) + \frac{\sigma\varepsilon}{2}|\nabla\phi|^2 \tag{11a}$$

$$W(\phi) = \frac{1}{4}(1 - \phi^2)^2, \tag{11b}$$

where $W = W(\phi)$ represents a double-well potential, ε represents an interface thickness variable and σ is a surface energy density coefficient. Additionally we choose a degenerate isotropic mobility tensor of the form:

$$\mathbf{M} = m\mathbf{I}, \tag{12a}$$

$$m(\phi) = \gamma(1 - \phi^2)^2, \tag{12b}$$

with $\gamma = \gamma(\varepsilon)$. This closes the Navier-Stokes Cahn-Hilliard system which reads:

$$\partial_t(\rho\mathbf{u} + \mathbf{J}) + \mathrm{div}\left(\rho^{-1}\left(\rho\mathbf{u} + \mathbf{J}\right) \otimes \left(\rho\mathbf{u} + \mathbf{J}\right)\right) + \nabla p + \phi\nabla\mu - \mathrm{div}\boldsymbol{\tau} - \rho\mathbf{g} = 0, \tag{13a}$$

$$\mathrm{div}\mathbf{u} = 0, \tag{13b}$$

$$\partial_t\phi + \mathbf{u} \cdot \nabla\phi - \mathrm{div}\left(m\nabla\left(\mu + \alpha p\right)\right) = 0, \tag{13c}$$

$$\mu - \frac{\sigma}{\varepsilon}W'(\phi) + \sigma\varepsilon\Delta\phi = 0. \tag{13d}$$

Remark 2.1 (Korteweg tensor)**.** *In many NSCH models the contribution of the surface forces appears in the momentum equation via a Korteweg type tensor. This is then often subsequently simplified for the Ginzburg-Landau free energy via the identity:*

$$\phi\nabla\mu = \mathrm{div}\left(\sigma\varepsilon\nabla\phi\otimes\nabla\phi + \left(\mu\phi - \frac{\sigma}{\varepsilon}W(\phi) - \frac{\sigma\varepsilon}{2}|\nabla\phi|^2\right)\mathbf{I}\right). \tag{14}$$

We remark here that this identity has nothing to do with the specific Ginzburg-Landau free energy as it holds in the general case $\Psi = \Psi(\phi, \nabla\phi)$:

$$\phi\nabla\mu = \mathrm{div}\left(\nabla\phi\otimes\frac{\partial\Psi}{\partial\nabla\phi} + (\mu\phi - \Psi)\mathbf{I}\right). \tag{15}$$

2.2. Physical properties

A physically vital feature of the NSCH model (13) is that it recovers the standard incompressible Navier-Stokes model in the single fluid regime.

Theorem 2.2 (Reduction to the incompressible Navier-Stokes equations)**.** *The NSCH model (13) reduces to the standard incompressible Navier-Stokes model in the single fluid regime ($\phi = \pm 1$).*

Proof. Noting that the mobility m is degenerate, the diffusive flux $\mathbf{J}$ vanishes in the single fluid regime. As a consequence, the symmetric velocity gradient reduces to $\mathbf{D} = \left(\nabla\mathbf{u} + (\nabla\mathbf{u})^T\right)/2$. Furthermore, the chemical potential μ vanishes in the single fluid regime. Taking these observations into account, we find that taking $\phi = \pm 1$ in (13) yields:

$$\partial_t\mathbf{u} + \mathrm{div}\left(\mathbf{u}\otimes\mathbf{u}\right) + \nabla\tilde{p} - \mathrm{div}\left(2\tilde{\nu}\mathbf{D}\right) - \mathbf{g} = 0, \tag{16a}$$

$$\mathrm{div}\mathbf{u} = 0, \tag{16b}$$

where $\tilde{p} = p/\rho$ and $\tilde{\nu} = \nu/\rho$ with constant density ρ, and $\mathbf{D} = \left(\nabla\mathbf{u} + (\nabla\mathbf{u})^T\right)/2$. $\qquad\square$

Remark 2.3 (Inconsistency single fluid regime)**.** *Not all exisiting NSCH models reduce to the incompressible Navier-Stokes equations in the single fluid regime. In particular, some models that employ a constant mobility parameter [3, 7–9] do not share this feature. As a result, inconsistencies can occur in this regime. For details we refer to ten Eikelder et al. [10].*

Theorem 2.4 (Conservation mixture mass and phase)**.** *The formulation conserves the mixture mass and the phase variable:*

$$\frac{\mathrm{d}}{\mathrm{d}t}\int_\Omega \rho \,\mathrm{d}\Omega = 0, \tag{17a}$$

$$\frac{\mathrm{d}}{\mathrm{d}t}\int_\Omega \phi \,\mathrm{d}\Omega = 0. \tag{17b}$$

Proof. This follows from integration of the mixture mass and phase field evolution equations. $\qquad\square$

Let us denote the local kinetic, gravitational and global energy as:

$$\mathscr{K} = \frac{1}{2}\rho\|\mathbf{v}\|^2 = \frac{1}{2}\rho\|\mathbf{u} + \rho^{-1}\mathbf{J}\|^2, \tag{18a}$$

$$\mathscr{G} = \rho g y, \tag{18b}$$

$$\mathscr{E} = \int_\Omega \mathscr{K} + \mathscr{G} + \Psi \,\mathrm{d}\Omega, \tag{18c}$$

where we recall the identity $\mathbf{v} = \mathbf{u} + \rho^{-1}\mathbf{J}$. The mass equations and the mixture momentum equation of the NSCH model (13) imply the following global energy evolution.

Theorem 2.5 (Energy dissipation). *Let* $\mathbf{u}, p$ *and* ϕ *be smooth solutions of the strong form* (13). *The associated total energy* $\mathscr{E}$ *satisfies the dissipation inequality:*

$$\frac{\mathrm{d}}{\mathrm{d}t}\mathscr{E} = -\int_\Omega \nu(\phi)(2\mathbf{D} + \lambda(\mathrm{div}\mathbf{v})\mathbf{I}) : \nabla\mathbf{v} \,\mathrm{d}x$$
$$-\int_\Omega \nabla(\mu + \alpha p) \cdot (m\nabla(\mu + \alpha p)) \,\mathrm{d}x + \mathscr{B} \leq 0 + \mathscr{B}, \tag{19}$$

where $\mathscr{B}$ *contains the boundary contributions:*

$$\mathscr{B} = \int_{\partial\Omega} \mathbf{n}^T \left(-p\mathbf{v} + \nu(\phi)(2\mathbf{D} + \lambda(\mathrm{div}\mathbf{v})\mathbf{I})\mathbf{v} - \frac{\partial\Psi}{\partial\nabla\phi}\left(\partial_t\phi + \mathbf{v}\cdot\nabla\phi\right) + (\mu + \alpha p)m\nabla(\mu + \alpha p)\right) \,\mathrm{d}a, \tag{20}$$

and where we recall $\mathbf{v} = \mathbf{u} + \rho^{-1}\mathbf{J}$.

Proof. See ten Eikelder et al. [10]. $\qquad\square$

Remark 2.6 (Viscous term). *The viscous term in* (19) *is negative by means of the well-known identity:*

$$-\nu(2\mathbf{D} + \lambda\mathrm{div}\mathbf{v}\mathbf{I}) : \nabla\mathbf{v} = -2\nu\left(\mathbf{D} - \frac{1}{d}\left(\mathrm{div}\mathbf{v}\right)\mathbf{I}\right) : \left(\mathbf{D} - \frac{1}{d}\left(\mathrm{div}\mathbf{v}\right)\mathbf{I}\right) - \nu\left(\lambda + \frac{2}{d}\right)(\mathrm{div}\mathbf{v})^2 \leq 0. \tag{21}$$

Remark 2.7 (Second law). *Even though this energy dissipation property is arguably favorable from the analytical and numerically perspective, it is not equivalent to the second law of thermodynamics. Unfortunately, in many articles the energy dissipation property is incorrectly referred to as the second law. The second law involves individual constituent quantities, whereas Theorem 2.5 contains mixture quantities that do not match the superposition of the constituent quantities. For more details we refer to [10, 13].*

Remark 2.8 (Second law). *The NSCH model is not the sole model for non-matching density flows with an energy-dissipation property. It can be shown that the (diffuse-interface) level-set model (together with a particular discretization) shares this feature [18].*

Next, we focus on the equilibrium properties. The equilibrium (E) solution $(\mathbf{u}_E, p_E, \phi_E, \mu_E)$ of the model (13) is characterized by:

$$(\mathbf{u}_E, p_E, \phi_E) = \underset{(\mathbf{u}, p, \phi)}{\mathrm{argmin}} \,\mathscr{E}(\mathbf{u}, p, \phi), \tag{22}$$

where $\mu_E = (\sigma/\varepsilon)W'(\phi_E) - \sigma\varepsilon\Delta\phi_E$. Restricting to smooth solutions we have the equivalence:

$$(\mathbf{u}_E, p_E, \phi_E) = \underset{(\mathbf{u}, p, \phi, \mu)}{\mathrm{argmin}} \,\mathscr{E}(\mathbf{u}, p, \phi) \iff \frac{\mathrm{d}}{\mathrm{d}t}\mathscr{E}(\mathbf{u}_E, p_E, \phi_E) = 0. \tag{23}$$

Invoking Theorem 2.5 we arrive at the equilibrium conditions:

$$2\nu_E\left(\mathbf{D}_E - \frac{1}{d}\left(\mathrm{div}\mathbf{v}_E\right)\mathbf{I}\right) : \left(\mathbf{D}_E - \frac{1}{d}\left(\mathrm{div}\mathbf{v}_E\right)\mathbf{I}\right) = 0, \tag{24a}$$

$$\nu_E\left(\lambda + \frac{2}{d}\right)(\mathrm{div}\mathbf{v}_E)^2 = 0, \tag{24b}$$

$$m_E\nabla(\mu_E + \alpha p_E) \cdot \nabla(\mu_E + \alpha p_E) = 0, \tag{24c}$$

with $\nu_E = \nu(\phi_E)$, $\mathbf{D}_E = \mathbf{D}(\mathbf{u}_E, \phi_E, \mu_E)$ and $m_E = m(\phi_E)$. From (24a)-(24b) we deduce $\mathbf{v}_E = \mathrm{const}$, and hence the kinetic energy vanishes. Recalling the condition on the mobility tensor (6), the equilibrium condition (24c) implies $\mu_E + \alpha p_E = \mathrm{const}$. As a consequence, the diffusive flux $\mathbf{J}$ vanishes in equilibrium.

We now arrive at the equilibrium conditions:

$$\nabla p_E + \phi_E \nabla \mu_E - \rho_E \mathbf{g} = 0, \tag{25a}$$

$$\mu_E + \alpha p_E = \text{const}, \tag{25b}$$

where (25a) follows from the momentum balance law. In the trivial case of a pure fluid ($\phi = \pm 1$) we have $\mu_E = 0$ and retrieve the hydrostatic equilibrium pressure $p_E = -\rho_E gy + \text{const}$. We now deduce the equilibrium profile in the non-trivial mixture case ($-1 < \phi_E < 1$) in absence of gravitational forces ($\mathbf{g} = 0$). Inserting (25b) into (25a) we find

$$(1 - \alpha \phi_E) \nabla p_E = 0. \tag{26}$$

Since $1 - \alpha \phi_E \neq 0$ we find $p_E = \text{const}$. This is consistent with the observation that fluids at rest have a constant pressure. Subsequently from (25b) we find $\mu_E = \text{const}$. Noting that $\mu_E = 0$ in the pure phase we deduce $\mu_E = 0$. In the one-dimensional situation this condition is fulfilled by the well-known smooth profile:

$$\phi_E(s) = \tanh\left(\frac{s}{\varepsilon\sqrt{2}}\right), \tag{27}$$

where s denotes the spatial coordinate centered at the interface. One can easily verify that free energy of the profile (27) is zero, and thus the equilibrium solution is compatible with (23). Finally, we associate the surface energy density coefficient σ with the surface tension coefficient, denoted $\tilde{\sigma}$. In the one-dimensional situation the integral of the free energy across the interface yields:

$$\int_{\mathbb{R}} \Psi(\phi_E) \, \mathrm{d}s = \sigma \frac{2\sqrt{2}}{3}. \tag{28}$$

We use the common practice to associate $\tilde{\sigma}$ with the one-dimensional free energy integral and set $\tilde{\sigma} = \sigma \frac{2\sqrt{2}}{3}$.

2.3. Non-dimensional form

We re-scale the system (9) based on the following dimensionless variables:

$$\mathbf{x}^* = \frac{\mathbf{x}}{X_0}, \quad t^* = \frac{t}{T_0}, \quad \mathbf{u}^* = \frac{\mathbf{u}}{U_0}, \quad \rho^* = \frac{\rho}{\rho_1}, \quad \nu^* = \frac{\nu}{\nu_1},$$

$$p^* = \frac{p}{\rho_1 U_0^2}, \quad \mu^* = \frac{\mu}{\rho_1 U_0^2}, \quad m^* = \frac{m\rho_1 U_0}{X_0}, \tag{29}$$

where X_0, T_0 and U_0 are characteristic length, time and velocity scales, respectively, related via $U_0 = X_0/T_0$. The dimensionless system reads:

$$\partial_t(\rho\mathbf{u} + \mathbf{J}) + \text{div}\left(\rho^{-1}\left(\rho\mathbf{u} + \mathbf{J}\right) \otimes \left(\rho\mathbf{u} + \mathbf{J}\right)\right) + \nabla p + \phi\nabla\mu - \frac{1}{\mathbb{R}\text{e}}\text{div}\boldsymbol{\tau} + \frac{1}{\mathbb{F}\text{r}^2}\rho\boldsymbol{j} = 0, \tag{30a}$$

$$\text{div}\mathbf{u} = 0, \tag{30b}$$

$$\partial_t\phi + \mathbf{u} \cdot \nabla\phi - \text{div}\left(m\nabla(\mu + \alpha p)\right) = 0, \tag{30c}$$

$$\mu - \frac{1}{\mathbb{W}\text{e}\mathbb{C}\text{n}}W'(\phi) + \frac{\mathbb{C}\text{n}}{\mathbb{W}\text{e}}\Delta\phi = 0, \tag{30d}$$

where we have omitted the $*$ symbols. The dimensionless coefficients are the Reynolds number ($\mathbb{Re}$), the Weber number ($\mathbb{We}$), the Froude number ($\mathbb{Fr}$) and the Cahn number ($\mathbb{Cn}$) given by:

$$\mathbb{Re} = \frac{\rho_1 U_0 X_0}{\nu_1}, \tag{31a}$$

$$\mathbb{We} = \frac{\rho_1 U_0^2 X_0}{\sigma}, \tag{31b}$$

$$\mathbb{Fr} = \frac{U_0}{\sqrt{g X_0}}, \tag{31c}$$

$$\mathbb{Cn} = \frac{\varepsilon}{X_0}. \tag{31d}$$

The kinetic, gravitational, and free energy take the form:

$$\mathscr{K} = \frac{1}{2}\rho\|\mathbf{v}\|^2 = \frac{1}{2}\rho\|\mathbf{u} + \rho^{-1}\mathbf{J}\|^2, \tag{32}$$

$$\mathscr{G} = \frac{1}{\mathbb{Fr}^2}\rho(\phi)y, \tag{33}$$

$$\Psi = \frac{\mathbb{Cn}}{2\mathbb{We}}\nabla\phi \cdot \nabla\phi + \frac{1}{\mathbb{We}\mathbb{Cn}}W(\phi). \tag{34}$$

The one-dimensional interface profile (in absence of gravitational forces) reads in non-dimensional form:

$$\phi(s) = \tanh\left(\frac{s}{\mathbb{Cn}\sqrt{2}}\right), \tag{35}$$

where s is a non-dimensional spatial coordinate centered at the origin.

3. Numerical methodology

In this section we present the numerical method for the consistent NSCH model. First we discuss the weak formulation in Section 3.1. Next, we present the isogeometric spatial discretization in Section 3.2, and subsequently the temporal discretization in Section 3.3.

3.1. Weak formulation

We base the methodology on the NSCH model formulated using the volume-averaged velocity as fundamental variable, as presented in the dimensionless form in (30). We denote the divergence-conforming trial solution space as $\mathcal{W}_T = \mathcal{V}_T \times \mathcal{Q}_T^3$, where $\mathcal{V}_T$ denotes the trail solution space for $\mathbf{u} = \mathbf{u}(t)$, and $\mathcal{Q}_T$ for $p = p(t), \phi = \phi(t)$ and $\mu = \mu(t)$. The corresponding divergence-conforming test function space denotes $\mathcal{W} = \mathcal{V} \times \mathcal{Q}^3$. The weak formulation takes the form:

Find $(\mathbf{u}, p, \phi, \mu) \in \mathcal{W}_T$ such that for all $(\mathbf{w}, q, \psi, \zeta) \in \mathcal{W}$:

$$(\mathbf{w}, \partial_t(\rho\mathbf{u} + \mathbf{J}))_\Omega - (\nabla\mathbf{w}, \rho^{-1}(\rho\mathbf{u} + \mathbf{J}) \otimes (\rho\mathbf{u} + \mathbf{J}))_\Omega - (\mathrm{div}\mathbf{w}, p)_\Omega + (\mathbf{w}, \phi\nabla\mu)_\Omega$$
$$+ \frac{1}{\mathbb{Re}}(\nabla\mathbf{w}, \boldsymbol{\tau})_\Omega + \frac{1}{\mathbb{Fr}^2}(\mathbf{w}, \rho\boldsymbol{j})_\Omega = 0, \tag{36a}$$

$$(q, \mathrm{div}\mathbf{u})_\Omega = 0, \tag{36b}$$

$$(\psi, \partial_t\phi)_\Omega + (\psi, \mathbf{u} \cdot \nabla\phi)_\Omega + (\nabla\psi, m\nabla(\mu + \alpha p))_\Omega = 0, \tag{36c}$$

$$(\zeta, \mu)_\Omega - \left(\nabla\zeta, \frac{\mathbb{Cn}}{\mathbb{We}}\nabla\phi\right)_\Omega - \left(\zeta, \frac{1}{\mathbb{Cn}\mathbb{We}}W'(\phi)\right)_\Omega = 0, \tag{36d}$$

where $\mathbf{J} = -(\rho_1 - \rho_2)m\nabla(\mu + \alpha p)/2$.

9

3.2. Spatial discretization

We apply the finite element/isogeometric analysis methodology. The parametric domain is defined as $\hat{\Omega} := (-1,1)^d \subset \mathbb{R}^d$, and $\mathcal{M}$ denotes the associated mesh. The parametric domain maps via the continuously differentiable geometrical map (with continuously differentiable inverse) $\mathbf{F} : \hat{\Omega} \to \Omega$ to the physical domain $\Omega \subset \mathbb{R}^d$. Similarly, the parametric mesh $\mathcal{M}$ maps to the corresponding physical mesh via:

$$\mathcal{K} = \mathbf{F}(\mathcal{M}) := \{\Omega_K : \Omega_K = \mathbf{F}(Q), Q \in \mathcal{M}\}. \tag{37}$$

Let $\mathbf{J_x} = \partial\mathbf{x}/\partial\boldsymbol{\xi}$ denote the Jacobian of the mapping $\mathbf{F}$. The parametric mesh size is its diagonal length, $h_Q = \mathrm{diag}(Q)$ for $Q \in \mathcal{M}$, and the associated physical mesh size h_K is:

$$h_K^2 := \frac{h_Q^2}{d} \|\mathbf{J_x}\|_F^2. \tag{38}$$

Here we recall that d denotes the number of physical dimensions, and we use the subscript F to denote the Frobenius norm. The (objective) Frobenius norm of the Jacobian equals:

$$\|\mathbf{J_x}\|_F^2 = \mathrm{Tr}\left(\mathbf{G}^{-1}\right), \tag{39}$$

where Tr denotes the trace operator. Here the element metric tensor and its inverse are:

$$\mathbf{G} = \mathbf{J_x}^{-T}\mathbf{J_x}^{-1}, \tag{40a}$$

$$\mathbf{G}^{-1} = \mathbf{J_x}\mathbf{J_x}^T. \tag{40b}$$

We now introduce the discrete isogeometric test function space $\mathcal{W}^h \subset \mathcal{W}$ and time-dependent solution space $\mathcal{W}_T^h \subset \mathcal{W}_T$ spanned by NURBS basis functions. The superscript h indicates that the space is finite-dimensional. Both the test function space and solution space are divergence-conforming, and we take $\mathcal{W}^h := \mathcal{V}^h \times (\mathcal{Q}^h)^3$ and $\mathcal{W}_T^h := \mathcal{V}_T^h \times (\mathcal{Q}_T^h)^3$. For details of the construction we refer to Evans and Hughes [19]. Applying the continuous Galerkin method now results in the semi-discrete approximation of (13):

Find $(\mathbf{u}^h, p^h, \phi^h, \mu^h) \in \mathcal{W}_T^h$ *such that for all* $(\mathbf{w}^h, q^h, \psi^h, \zeta^h) \in \mathcal{W}^h$:

$$(\mathbf{w}^h, \partial_t(\rho^h\mathbf{u}^h + \mathbf{J}^h))_\Omega - (\nabla\mathbf{w}^h, (\rho^h)^{-1}(\rho^h\mathbf{u}^h + \mathbf{J}^h) \otimes (\rho^h\mathbf{u}^h + \mathbf{J}^h))_\Omega$$
$$-(\mathrm{div}\mathbf{w}^h, p)_\Omega + \left(\mathbf{w}^h, \phi^h\nabla\mu^h\right)_\Omega + (\nabla\mathbf{w}^h, \boldsymbol{\tau}^h)_\Omega + \frac{1}{\mathbb{F}\mathrm{r}^2}\left(\mathbf{w}^h, \rho^h\boldsymbol{\jmath}\right)_\Omega = 0, \tag{41a}$$

$$(q^h, \mathrm{div}\mathbf{u}^h)_\Omega = 0, \tag{41b}$$

$$\left(\psi^h, \partial_t\phi^h\right)_\Omega + \left(\psi^h, \mathbf{u}^h \cdot \nabla\phi^h\right)_\Omega + \frac{1}{\mathbb{W}\mathrm{e}}\left(\nabla\psi, m\nabla\left(\mu^h + \alpha p^h\right)\right)_\Omega = 0, \tag{41c}$$

$$\left(\zeta^h, \mu^h\right)_\Omega - \left(\nabla\zeta^h, \frac{\mathbb{C}\mathrm{n}}{\mathbb{W}\mathrm{e}}\nabla\phi^h\right)_\Omega - \left(\zeta^h, \frac{1}{\mathbb{C}\mathrm{n}\mathbb{W}\mathrm{e}}W'(\phi^h)\right)_\Omega = 0, \tag{41d}$$

where $\mathbf{u}^h(0) = \mathbf{u}_0^h$, $\phi^h(0) = \phi_0^h$ and $p^h(0) = p_0^h$ in Ω, $\rho^h = \rho(\phi^h)$, $\boldsymbol{\tau}^h = \boldsymbol{\tau}(\mathbf{u}^h, p^h, \phi^h, \mu^h)$, $\mathbf{J}^h = \mathbf{J}(p^h, \phi^h, \mu^h)$ and $m^h = m(\phi^h)$. The semi-discrete formulation (41) reduces to the standard (weak) form of the incompressible Navier-Stokes equations in the single fluid regime. Additionally, it inherits the conservation property from Theorem 2.4 and has pointwise divergence-free velocities.

Theorem 3.1 (Properties semi-discrete formulation). *Let* $(\mathbf{u}^h, p^h, \phi^h, \mu^h)$ *be a smooth solution of the semi-discrete formulation* (41). *The formulation has the properties:*

1. *It conserves the global mass and the global phase field:*

$$\frac{\mathrm{d}}{\mathrm{d}t} \int_{\Omega} \rho^h \, \mathrm{d}\Omega = 0, \tag{42a}$$

$$\frac{\mathrm{d}}{\mathrm{d}t} \int_{\Omega} \phi^h \, \mathrm{d}\Omega = 0. \tag{42b}$$

2. *It has pointwise divergence-free velocities:*

$$\mathrm{div}\mathbf{u}^h \equiv 0. \tag{43}$$

Proof. 1. Phase conservation follows from taking $\psi^h = 1$ in the phase field equation (41c). Mass conservation subsequently follows from the observation that ρ^h is an affine function of ϕ^h.

2. Since $\nabla \cdot \mathbf{u}^h \in \mathcal{Q}_T^h$ we can substitute this weighting function choice into (41b):

$$0 = \left(\mathrm{div}\mathbf{u}^h, \mathrm{div}\mathbf{u}^h\right)_{\Omega} \quad \Rightarrow \quad \mathrm{div}\mathbf{u}^h \equiv 0 \quad \text{in } \Omega. \tag{44}$$

$\square$

Remark 3.2 (Energy-dissipation). *The formulation* (41) *does not inherit the energy-dissipation property of Theorem 2.5. This is a consequence of the observation that the weighting function that would lead to an energy-dissipation statement is not a member of $\mathcal{W}^h$.*

3.3. Temporal discretization

To introduce the time-discretization we first subdivide the time domain $\mathcal{T}$ into elements $\mathcal{T}_n = (t_n, t_{n+1})$ of size $\Delta t_n = t_{n+1} - t_n$ with time level $n = 0, 1, ..., N$. We make use of the conventional notation of indicating the time level of a discrete quantity with a subscript, e.g. $\mathbf{u}_n^h, p_n^h, \phi_n^h$ and μ_n^h denote the discrete velocity $\mathbf{u}^h$, pressure p^h, phase field ϕ^h and chemical potential μ^h at time level n. We write $[\![\mathbf{a}^h]\!]_n := \mathbf{a}_{n+1}^h - \mathbf{a}_n^h$ for the jump of the vector quantity $\mathbf{a}^h$. The intermediate time-levels and associated time derivatives are given by:

$$\mathbf{u}_{n+1/2}^h := \tfrac{1}{2}(\mathbf{u}_n^h + \mathbf{u}_{n+1}^h), \qquad \frac{1}{\Delta t_n}[\![\mathbf{u}^h]\!]_n := \frac{1}{\Delta t_n}(\mathbf{u}_{n+1}^h - \mathbf{u}_n^h), \tag{45a}$$

$$\phi_{n+1/2}^h := \tfrac{1}{2}(\tilde{\phi}_n^h + \phi_{n+1}^h), \qquad \frac{1}{\Delta t_n}[\![\phi^h]\!]_n := \frac{1}{\Delta t_n}(\phi_{n+1}^h - \tilde{\phi}_n^h) \tag{45b}$$

$$\rho_{n+1/2}^h := \rho(\phi_{n+1/2}^h), \qquad \frac{1}{\Delta t_n}[\![\rho^h]\!]_n := \frac{1}{\Delta t_n}(\rho_{n+1}^h - \rho_n^h), \tag{45c}$$

$$\mathbf{J}_{n+1/2}^h := \mathbf{J}(p_{n+1/2}^h, \phi_{n+1/2}^h, \mu_{n+1/2}^h), \qquad \frac{1}{\Delta t_n}[\![\rho^h \mathbf{u}^h]\!]_n := \frac{1}{\Delta t_n}\left(\rho_{n+1}^h \mathbf{u}_{n+1}^h - \rho_n^h \mathbf{u}_n^h\right), \tag{45d}$$

$$\frac{1}{\Delta t_n}[\![\mathbf{J}^h]\!]_n := \frac{1}{\Delta t_n}\left(\mathbf{J}_{n+1}^h - \mathbf{J}_n^h\right), \tag{45e}$$

where we define $\tilde{\phi}_n^h = \phi_n^h$ for $|\phi_n^h| \leq 1$, and $\tilde{\phi}_n^h = 1$ (respectively -1) for $\phi_n^h > 1$ (respectively $\phi_n^h < -1$). This permits working with large density and viscosity ratios. We additionally define

$$\rho_n^h := \rho(\tilde{\phi}_n^h), \qquad\qquad\qquad \rho_{n+1}^h = \rho(\phi_{n+1}^h) \tag{46a}$$

$$m_n^h := m(\tilde{\phi}_n^h), \qquad\qquad\qquad m_{n+1}^h := m(\phi_{n+1}^h) \tag{46b}$$

$$\mathbf{J}_n^h := \mathbf{J}(p_n^h, \tilde{\phi}_n^h, \mu_n^h), \qquad\qquad \mathbf{J}_{n+1}^h := \mathbf{J}(p_{n+1}^h, \phi_{n+1}^h, \mu_{n+1}^h), \tag{46c}$$

$$W'^h_{n+1/2} = W'(\phi_{n+1/2}^h) \tag{46d}$$

$$\mathbf{D}_{n+1/2}^h = \nabla^s \left(\mathbf{u}_{n+1/2}^h + (\rho_n^h)^{-1} \mathbf{J}_{n+1/2}^h \right) \tag{46e}$$

$$\boldsymbol{\tau}_{n+1/2}^h = \nu(\phi_{n+1/2}^h) \left(2\mathbf{D}_{n+1/2}^h + \lambda \mathrm{div}\left((\rho_n^h)^{-1} \mathbf{J}_{n+1/2}^h \right) \mathbf{I} \right), \tag{46f}$$

Furthermore, the separate pressure and chemical potential terms are taken at time level $n+1$. The temporal discretization of the remaining terms uses the midpoint scheme. The method in fully-discrete form now reads:

Given $\mathbf{u}_n^h, p_n^h, \phi_n^h$ and μ_n^h, find $\mathbf{u}_{n+1}^h, p_{n+1}^h, \phi_{n+1}^h$ and μ_{n+1}^h such that for all $(\mathbf{w}^h, q^h, \psi^h, \zeta^h) \in \mathcal{W}_{0,h}$:

$$\left(\mathbf{w}^h, \frac{[\![\rho^h \mathbf{u}^h + \mathbf{J}^h]\!]_n}{\Delta t_n} \right)_\Omega - (\mathrm{div}\mathbf{w}^h, p_{n+1}^h)_\Omega + \left(\mathbf{w}^h, \phi_{n+1/2}^h \nabla \mu_{n+1}^h \right)_\Omega$$

$$-(\nabla \mathbf{w}^h, \rho_{n+1/2}^h \mathbf{u}_{n+1/2}^h \otimes \mathbf{u}_{n+1/2}^h + \mathbf{u}_{n+1/2}^h \otimes \mathbf{J}_{n+1/2}^h + \mathbf{J}_{n+1/2}^h \otimes \mathbf{u}_{n+1/2}^h)_\Omega$$

$$+((\rho_n^h)^{-1} \mathbf{J}_{n+1/2}^h \otimes \mathbf{J}_{n+1/2}^h)_\Omega + (\nabla \mathbf{w}^h, \boldsymbol{\tau}_{n+1/2}^h)_\Omega + \frac{1}{\mathbb{F}\mathrm{r}^2}(\mathbf{w}^h, \rho_{n+1/2}^h \boldsymbol{f})_\Omega = 0, \tag{47a}$$

$$(q^h, \mathrm{div}\mathbf{u}_{n+1/2}^h)_\Omega = 0, \tag{47b}$$

$$\left(\psi^h, \frac{[\![\phi^h]\!]_n}{\Delta t_n} \right)_\Omega + (\psi^h, \mathbf{u}_{n+1/2}^h \cdot \nabla \phi_{n+1/2}^h)_\Omega + \frac{1}{\mathbb{W}\mathrm{e}} \left(\nabla \psi^h, m_{n+1/2}^h \nabla \left(\mu_{n+1}^h + \alpha p_{n+1}^h \right) \right)_\Omega = 0, \tag{47c}$$

$$\left(\zeta^h, \mu_{n+1}^h \right)_\Omega - \frac{\mathbb{C}\mathrm{n}}{\mathbb{W}\mathrm{e}} \left(\nabla \zeta^h, \nabla \phi_{n+1/2}^h \right)_\Omega - \frac{1}{\mathbb{C}\mathrm{n}\mathbb{W}\mathrm{e}} \left(\zeta^h, W'^h_{n+1/2} \right)_\Omega = 0. \tag{47d}$$

Theorem 3.3 (Fully-discrete divergence-free velocities). *The algorithm* (47) *has pointwise divergence-free solutions:*

$$\mathrm{div}\mathbf{u}_{n+1/2}^h \equiv 0. \tag{48}$$

The proof is analogously to the semi-discrete case.

4. Comparison with existing models

In this section we verify the computational setup via two-dimensional buoyancy-driven rising bubble problems. The simulation of bubble dynamics problems involves all aspects of the Navier-Stokes Cahn-Hilliard model (i.e. inertia, viscous forces, gravity, and surface tension effects). In this benchmark problem a bubble of (lighter) fluid 2 with initial diameter $D_0 = 2R_0 = 0.5$ is placed in the rectangular domain $[0, 1] \times [0, 2]$ at location $(0.5, 0.5)$ in (heavier) fluid 1 [20]. The initial phase field profile is:

$$\phi_0^h(\mathbf{x}) = \tanh \frac{\sqrt{(x - 0.5)^2 + (y - 0.5)^2} - R_0}{\mathbb{C}\mathrm{n}\sqrt{2}}. \tag{49}$$

At the left and right boundaries a no-penetration boundary condition ($\mathbf{u} \cdot \mathbf{n} = 0$) is applied, and at the top and bottom boundary a no-slip boundary condition ($\mathbf{u} = 0$) is enforced. A sketch of the problem setup is given in Figure 1.
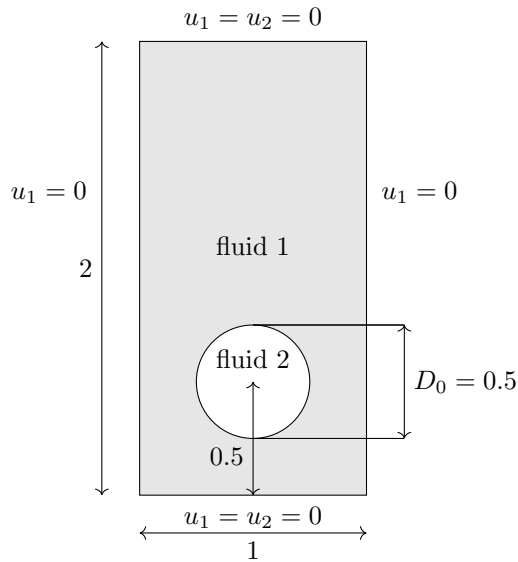
Figure 1: Situation sketch cases 1 and 2

The motion of rising bubble problems is typically described by the Archimedes number ($\mathbb{A}\mathrm{r}$) and the Eötvös number ($\mathbb{E}\mathrm{o}$) since the Reynolds number is a priori unknown. The Archimedes number measures the relative importance of buoyancy to viscous forces, and the Eötvös number describes the relative importance of gravity and surface tension. The Eötvös number is also known as the Bond number. We select as reference values (see (29)):

$$X_0 = D_0 \tag{50a}$$

$$U_0 = \frac{D_0}{T_0} \tag{50b}$$

$$T_0 = \sqrt{\frac{\rho_1 D_0^3}{\sigma}}, \tag{50c}$$

where T_0 is the capilary time scale. As a consequence the dimensionless numbers (Section 2.3) become:

$$\mathbb{Re} = \mathbb{Eo}^{-1/2}\mathbb{Ar}, \tag{51a}$$

$$\mathbb{Fr} = \mathbb{Eo}^{-1/2}, \tag{51b}$$

$$\mathbb{We} = 1, \tag{51c}$$

where the Archimedes number ($\mathbb{Ar}$) and the Eötvös number ($\mathbb{Eo}$) are given by:

$$\mathbb{Ar} = \frac{\rho_1\sqrt{gD_0^3}}{\nu_1}, \tag{52a}$$

$$\mathbb{Eo} = \frac{\rho_1 g D_0^2}{\sigma}. \tag{52b}$$

The system is now characterized by 5 dimensionless quantities: $\mathbb{Ar}$, $\mathbb{Eo}$, $\mathbb{Cn}$, ρ_1/ρ_2, ν_1/ν_2. The benchmark problem involves two cases which are described by different parameter values in Table 2. All computations were performed on a rectangular uniform mesh with physical element sizes $h = h_K = 1/16, 1/32, 1/64, 1/128$. The computations employ basis functions that are mostly C^0-linear, however every velocity space is enriched to be quadratic C^1 in the associated direction. The time step size is taken as $\Delta t_n = 0.128h$, and the Cahn number as $\mathbb{Cn} = 1.28h$.

Case	ρ_1	ρ_2	μ_1	μ_2	σ	g	$\mathbb{Ar}$	$\mathbb{Eo}$
1	1000	100	10	1	24.5	0.98	35	10
2	1000	1	1	0.1	1.96	0.98	35	125

Table 2: Parameters for the two-dimensional rising bubble cases.

Figures 2 and 3 show the zero phase field ($\phi = 0$) contours for cases 1 and 2, respectively. We see that the deformation of the bubble is rather small in case 1, whereas in case 2 we observe significant deformation. In both cases, there are almost no visible differences between the results of the finest two meshes. For a quantitative comparison with reference results from the literature, we use the the center of mass (y_b) and rise velocity (v_b) defined as:

$$y_b := \frac{\int_{\phi<0} y \ \mathrm{d}x}{\int_{\phi<0} \ \mathrm{d}x}, \tag{53a}$$

$$v_b := \frac{\int_{\phi<0} u_2 \ \mathrm{d}x}{\int_{\phi<0} \ \mathrm{d}x}. \tag{53b}$$

(a) $h = 1/128$, $t = 0, 1, 2, 3$
in orange, red, green and blue (resp).

(b) $t = 3$, $h = 1/16, 1/32, 1/64, 1/128$
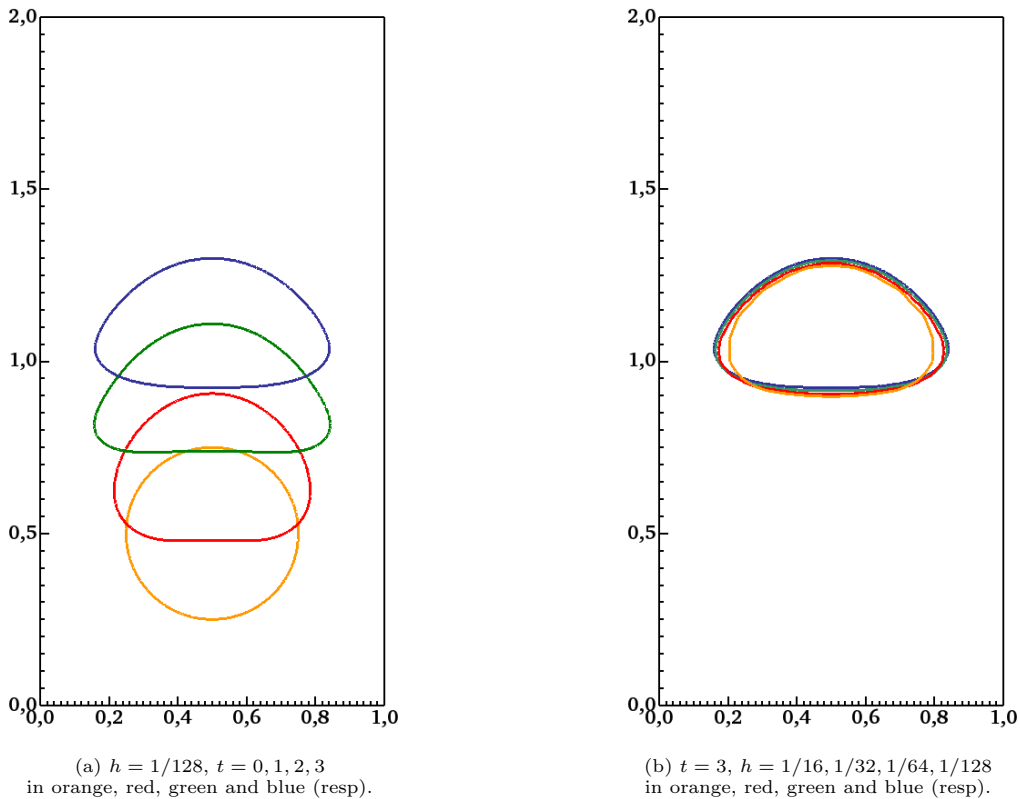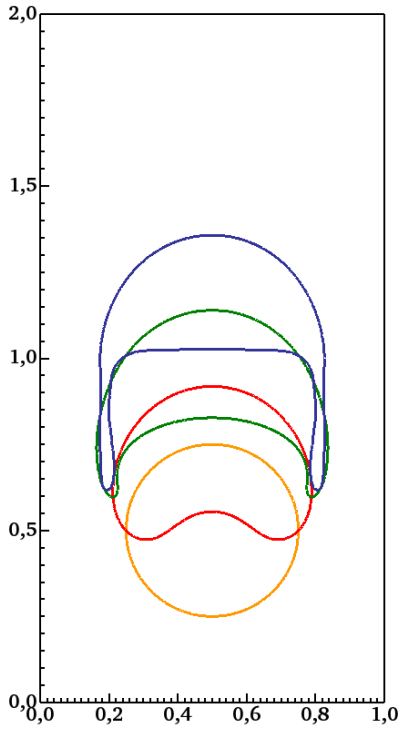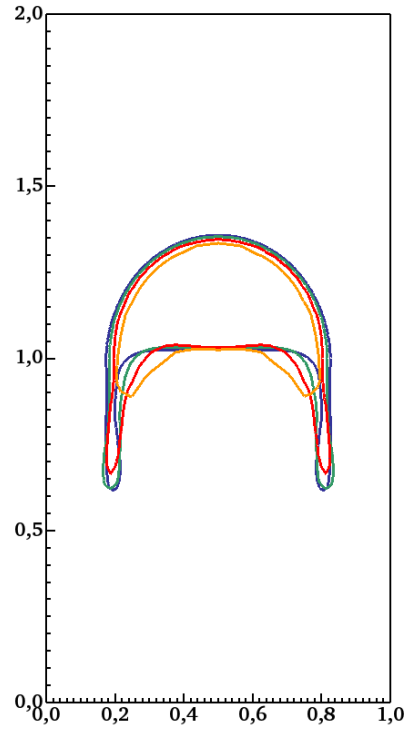in orange, red, green and blue (resp).

Figure 2: Case 1. Contours of the phase field $\phi = 0$, (a) different time instances, (b) different mesh sizes.

In Figures 4 to 7 we plot for the two cases (i) the center of mass and (ii) the rise velocity, for different mesh sizes, and relative to reference computational data. This data is obtained with (1) the TP2D code (2) the FreeLIFE code, (3) the MooNMD code, see [20], and the NSCH models of Abels et al. [6], Boyer [4] and Ding et al. [5]. The computations with the NSCH models were performed by Aland and Voigt [21]. The center of mass matches well with the reference data for both cases. Concerning the rise velocity, we observe significant difference for case 2 for $t > 1.5$. In this regime, our computational results agree quite well with the NSCH computations performed by Aland and Voigt [21], but not with the TP2D, FreeLIFE and MooNMD code results. We remark that both the physical models as well as the computational methods differ between the computational results. The NSCH model is an energy stable model with a diffuse interface, whereas the reference data of the TP2D, FreeLIFE and MooNMD codes is based on a level set description of the interface.

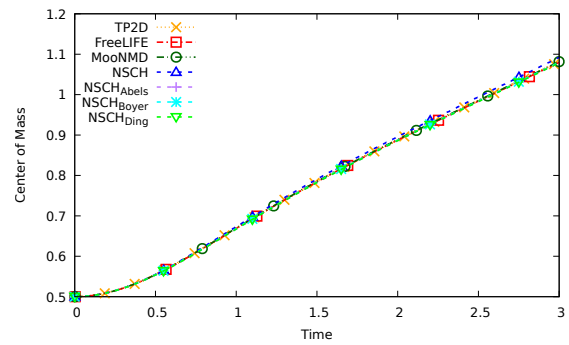(a) $h_K = 1/128$, $t = 0, 1, 2, 3$
in orange, red, green and blue (resp).

(b) $t = 3$, $h_K = 1/16, 1/32, 1/64, 1/128$
in orange, red, green and blue (resp).

Figure 3: Case 2. Contours of the phase field $\phi = 0$, (a) different time instances, (b) different mesh sizes.
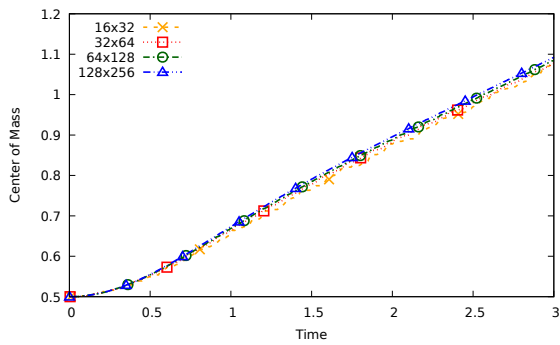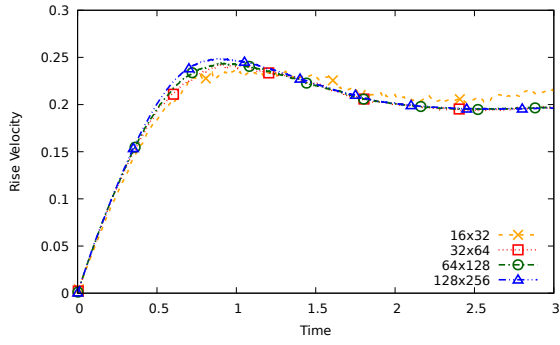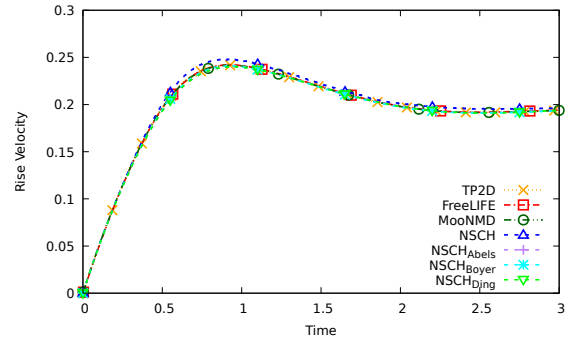

(a) $h_K = 1/16, 1/32, 1/64, 1/128$.

(b) Relative to reference data.

Figure 4: Case 1. Center of mass (a) for different mesh sizes, and (b) a comparison of the finest mesh results to reference data.
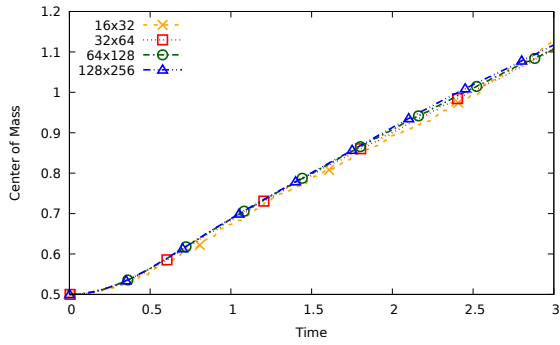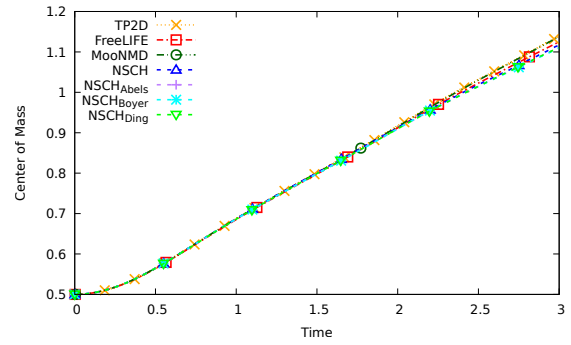
(a) $h_K = 1/16, 1/32, 1/64, 1/128$.

(b) Relative to reference data.

Figure 5: Case 1. Rise velocity (a) for different mesh sizes, and (b) a comparison of the finest mesh results to reference data.
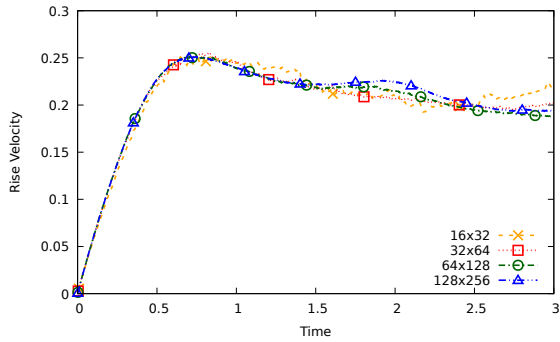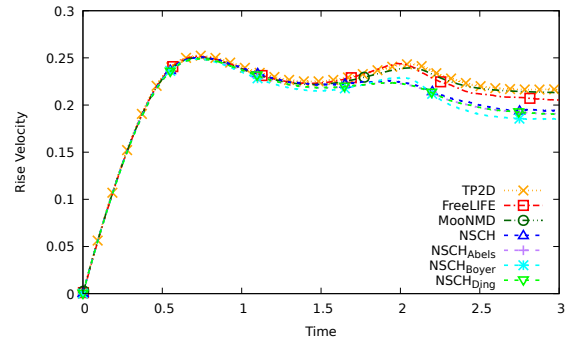

(a) $h = 1/16, 1/32, 1/64, 1/128$.

(b) Relative to reference data.

Figure 6: Case 2. Center of mass (a) for different mesh sizes, and (b) a comparison of the finest mesh results to reference data.

(a) $h_K = 1/16, 1/32, 1/64, 1/128$.

(b) Relative to reference data.

Figure 7: Case 2. Rise velocity (a) for different mesh sizes, and (b) a comparison of the finest mesh results to reference data.

5. Numerical benchmarks in three dimensions

In this section we simulate two benchmark problems to validate our consistent NSCH model against experimental data. We first study a buoyancy-driven rising bubble, and second the contraction of a liquid filament. Analogously to Section 4, all the implementations use basis functions that are mostly C^0-linear, but every velocity space is enriched to be quadratic C^1 in the associated direction. The system of equations is solved with the standard GMRES method with additive Schwartz preconditioning provided by Petsc [22].

5.1. Three-dimensional buoyancy-driven rising bubbles

The simulation of the three dimensional rising bubble problem is similar to the two-dimensional setup in Section 4. In particular we use the same reference values and definitions of the dimensionless parameters. In this validation case we consider an air bubble at 20°C in the water. The deforming bubble rises due to buoyancy, and after some time takes its final shape and velocity. The physical domain setup coincides with that of Yan et al. [23]: the bubble with initial diameter $D_0 = 2R_0 = 1$ is placed in the rectangular domain $[0, 12] \times [0, 24] \times [0, 12]$ at location $(6, 10.5, 6)$. The initial phase field profile is:

$$\phi_0^h(\mathbf{x}) = \tanh \frac{\sqrt{(x-6)^2 + (y-10.5)^2 + (z-6)^2} - R_0}{\mathbb{C}n\sqrt{2}}. \tag{54}$$

At all boundaries a no-penetration boundary condition ($\mathbf{u} \cdot \mathbf{n} = 0$) is applied. A sketch of the problem setup is given in Figure 8a.

(a) Setup   (b) Coarsest mesh, quarter of domain
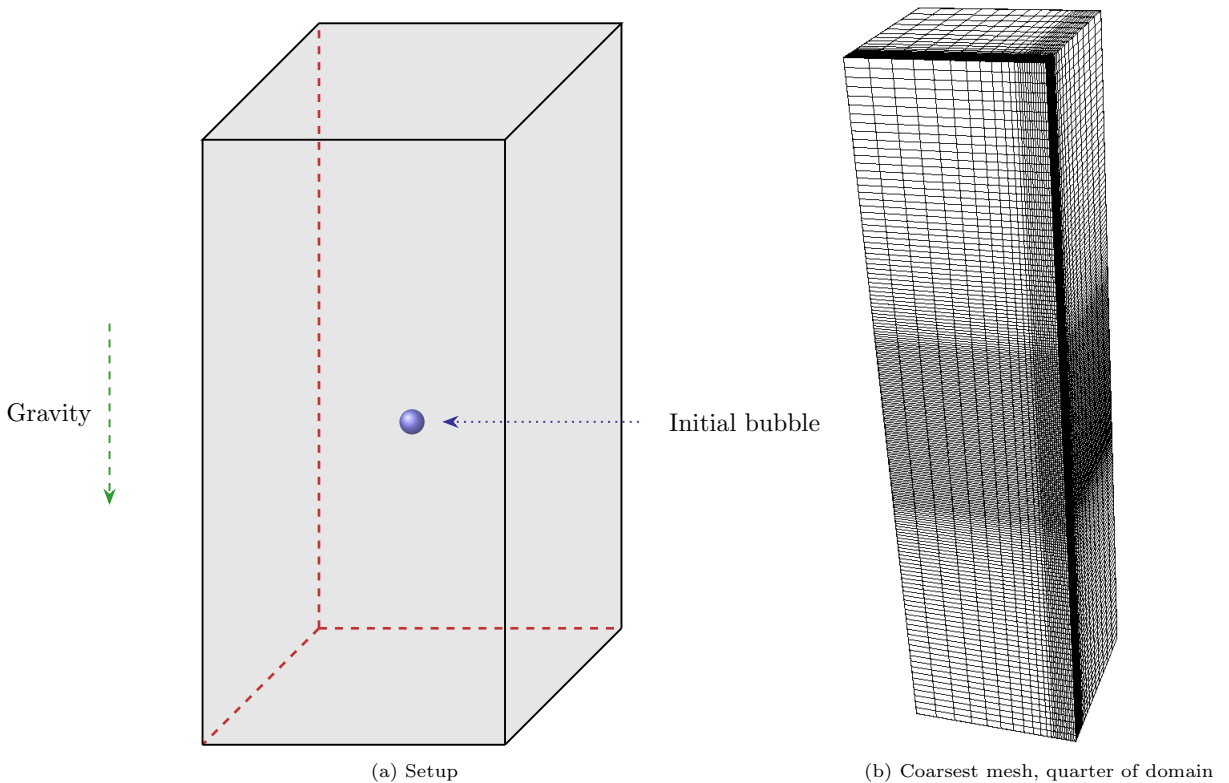
Figure 8: Three-dimensional rising bubble problem.

We note that the problem is symmetric in the planes $x = 6$ and $z = 6$. In order to reduce the computational effort, we only simulate the quarter $[0, 6] \times [0, 24] \times [0, 6]$ of the domain and apply symmetry boundary conditions. To accurately capture the bubble dynamics, we use a stretched single patch mesh with a uniform

mesh size $h = \min_K h_K$ inside the region of the bubble $[5.2, 6] \times [9, 15] \times [5.2, 6]$. The element size gradually increases towards the boundary of the computational domain, see Figure 8b.

The system is now characterized by 5 dimensionless quantities: $\mathbb{A}$r, $\mathbb{E}$o, $\mathbb{C}$n, ρ_1/ρ_2 and ν_1/ν_2. We consider three different cases, for which the dimensionless parameters are given in Table 3.

Case	ρ_1/ρ_2	ν_1/ν_2	$\mathbb{A}$r	$\mathbb{E}$o
1	1000	100	1.671	17.7
2	1000	100	15.24	243
3	1000	100	30.83	339

Table 3: Parameters for the three-dimensional rising bubble cases.

To preclude the influence of the unresolved flow features and domain boundaries, we compare computational results on different meshes. We compare the results of case 2 on a coarse mesh, a medium mesh, and a fine mesh with total number of elements: $24 \times 192 \times 24 = 110592$, $48 \times 384 \times 48 = 884736$, and $96 \times 768 \times 96 = 7077888$, with $h = 1/15, 1/30, 1/60$ respectively. We select the Cahn number as $\mathbb{C}$n $= 0.72h$ and the time step size as $\Delta t_n = 0.075h$. In Figure 9 we visualize the final bubble shape for the different meshes. We observe that the influence of the mesh is small when comparing the medium and fine mesh results. Figure 10 shows the Reynolds number of the bubble $(\rho_1 v_b D_0)/\nu_1$ for the three meshes. The results of the medium and fine mesh show negligible differences. In the following we work with the fine mesh discretization.
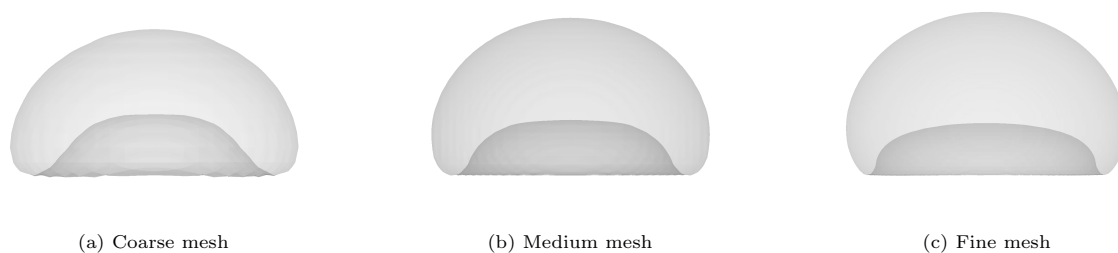

(a) Coarse mesh   (b) Medium mesh   (c) Fine mesh

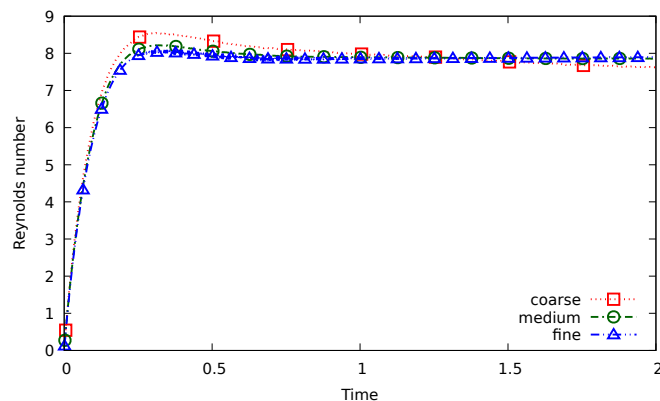Figure 9: Rising bubble problem. Case 2. Final bubble shape for different mesh sizes.

Figure 10: Case 2. Reynolds number for different meshes.

Case	Bhaga and Weber	Yan et al.	Hua et al.	Amaya-Bower and Lee	Current
1	0.232	0.2593	0.182		0.211
2	7.77	7.5862	7.605	6.2	7.90
3	18.3	18.1717	17.758	15.2	17.5

Table 4: Final Reynolds number for the three-dimensional rising bubble cases. Left to right: Bhaga and Weber [24], Yan et al. [23], Hua et al. [25], Amaya-Bower and Lee [26] and the current NSCH computation.

In Table 4 we show the final Reynolds numbers of each of the three cases, and visualize the final bubble shape in Figure 11. The table and figure include experimental data of Bhaga and Weber [24], and computational data Yan et al. [23], Hua et al. [25] and Amaya-Bower and Lee [26]. We observe that the bubble largely remains spherical in case 1, while in cases 2 and 3 a significant deformation is visible. In cases 1 and 2, we observe that the terminal Reynolds numbers computed by our methodology show the closest match with the experimental data. For case 3, all computational results show lower terminal Reynolds numbers than the experimental results. Concerning the final bubble shape, we see that bubble shape of our computation matches well with that of Yan et al. [23] and the experimental data [24]. Finally, to highlight the deformation differences among the three cases, we visualize the three-dimensional terminal bubble shapes in Figure 12.
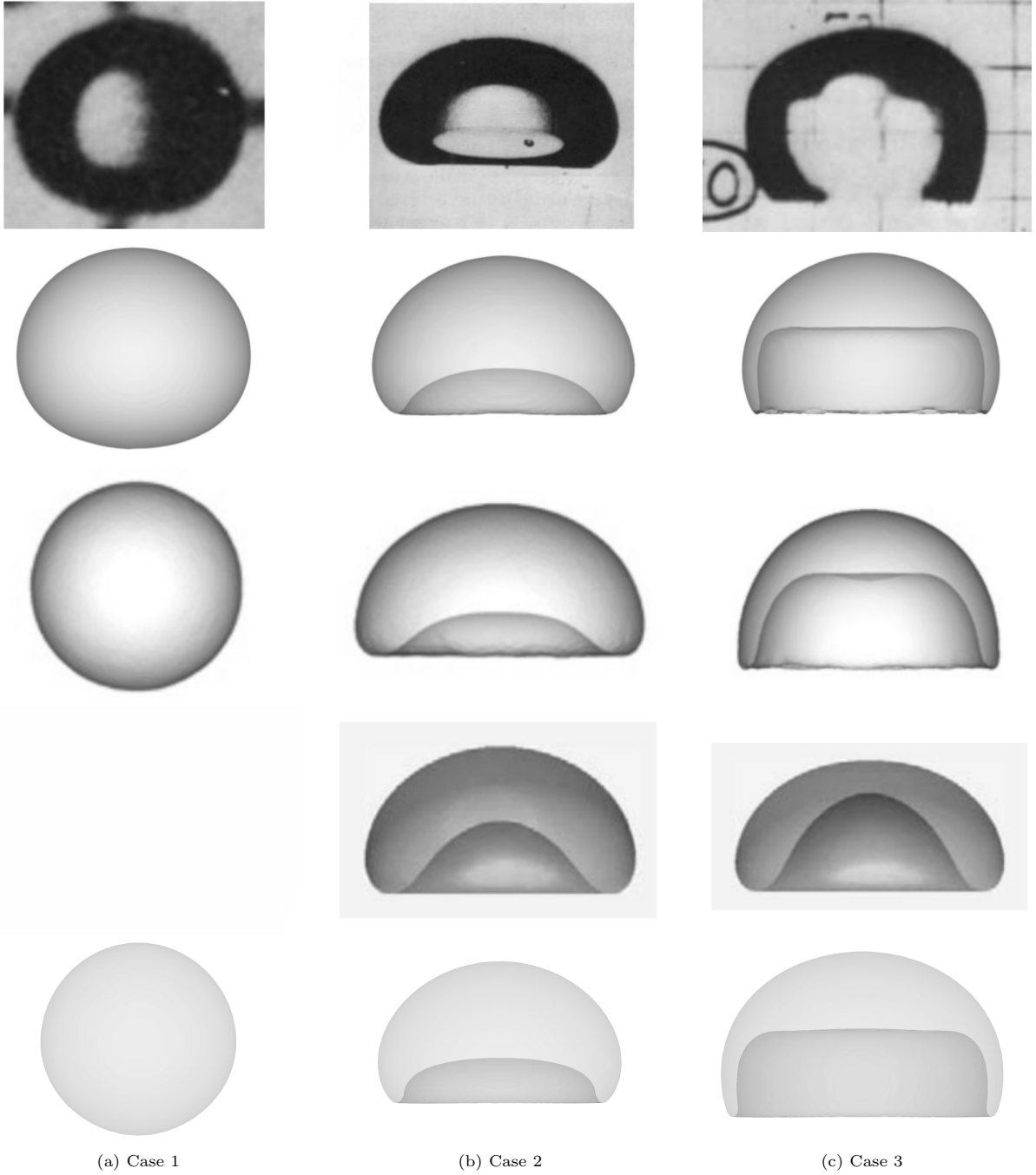
Figure 11: Rising bubble problem. Final bubble shape. Top to bottom: Bhaga and Weber [24], Yan et al. [23], Hua et al. [25], Amaya-Bower and Lee [26], and the current NSCH computation.
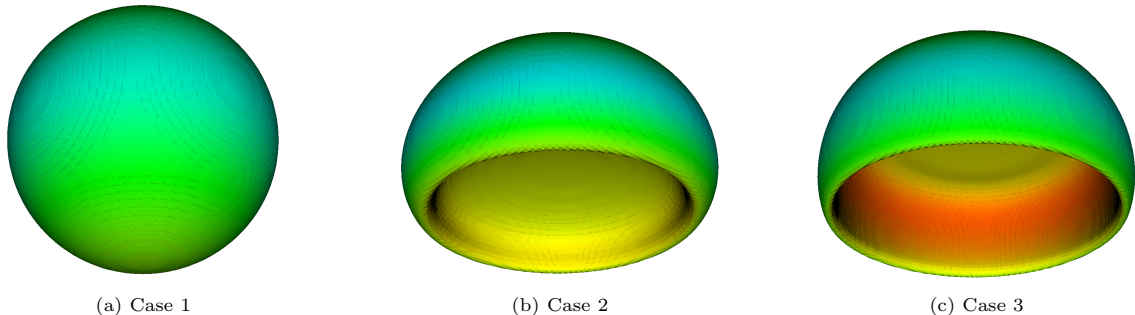
(a) Case 1   (b) Case 2   (c) Case 3

Figure 12: Rising bubble problem. Three-dimensional terminal bubble shape of the NSCH computations.

5.2. Three-dimensional liquid filament contraction

The dynamics of a contracting liquid filament is a fundamental problem that occurs in a wide range of problems in fluid dynamics, e.g. microfluidics, biological systems, spray, and inkjet printing. In this qualitative application case of a contracting liquid filament we validate our computational results against experimental data of Castrejon et al. [27]. The fate of a contracting cylindrical liquid filament depends on the Ohnesorge number $\mathbb{O}h$ (the relative importance of viscosity and surface tension) and the aspect ratio Γ_0. The aspect ratio is defined as $\Gamma_0 = L_0/D_0$ where L_0 is the initial length of the filament, and $D_0 = 2R_0$ the width, and R_0 the radius.

We use a rectangular physical domain rectangular domain of size $[0, 24] \times [0, 180] \times [0, 24]$ in which the liquid filament is placed at the center. The initial phase field profile is:

$$\phi_0^h(\mathbf{x}) = \begin{cases} \tanh \dfrac{R_0 - \sqrt{(x-12)^2 + (y-32)^2 + (z-12)^2}}{\mathbb{C}n\sqrt{2}} & \text{if } y < 32, \\[3mm] \tanh \dfrac{R_0 - \sqrt{(x-12)^2 + (z-12)^2}}{\mathbb{C}n\sqrt{2}} & \text{if } 32 < y < 148, \\[3mm] \tanh \dfrac{R_0 - \sqrt{(x-12)^2 + (y-148)^2 + (z-12)^2}}{\mathbb{C}n\sqrt{2}} & \text{if } 148 < y. \end{cases} \tag{55}$$

We applied at all boundaries the no-penetration boundary condition. Figure 13 shows the sketch of the problem setup.

Similar as in the case of the rising bubble, the problem is symmetric in the planes $x = 12$ and $z = 12$. In order to reduce the computational effort, we only simulate the quarter $[0, 12] \times [0, 180] \times [0, 12]$ of the domain and apply symmetry boundary conditions. Again, we use a stretched single patch mesh with a uniform mesh size $h = \min_K h_K$ inside the region of the ligament $[9, 12] \times [20, 160] \times [9, 12]$. We use a mesh with $16 \times 600 \times 16 = 153600$ elements with $h = 0.25$.

A liquid filament either remains a single filament or breaks up into possibly multiple smaller filaments. Considering filaments that are initially at rest, those that have a large $\mathbb{O}h$ and small Γ_0 typically remain a single body whereas filaments with small $\mathbb{O}h$ and large Γ_0 tend to break up. It is difficult in an experimental setup to ensure that a filament is initially completely at rest. To minimize the influence of start-up effects, we study the contraction of a long liquid filament.

We consider a pure water liquid filament at rest at $22°C$ in the air. The water viscosity is measured at $\nu_1 = 100 \times 10^{-3}$Pa s, and the water density is $\rho_1 = 1000 \times 10^3$g/m^3 and the gravitational constant is
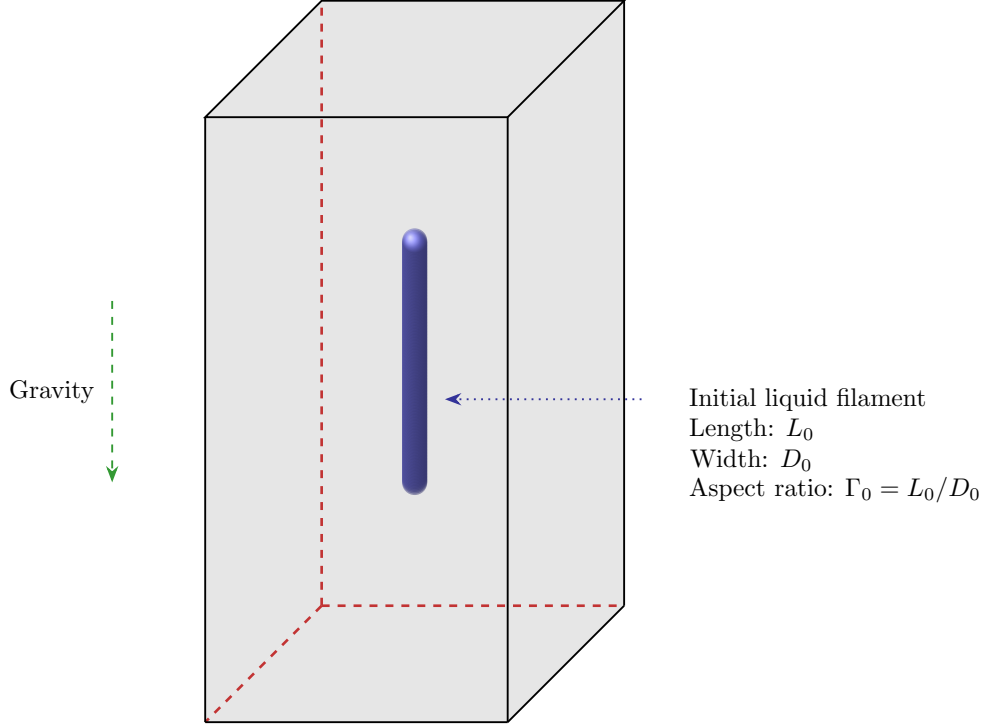
Figure 13: Setup of the liquid filament contraction problem.

$g = 9.81\text{m/s}^2$. The dimensions are $R_0 = 0.13 \times 10^{-3}\text{m}$ and $\Gamma_0 = 59$. We select as reference values:

$$X_0 = R_0, \tag{56a}$$

$$T_0 = \sqrt{\frac{\rho_1 R_0^3}{\sigma}}, \tag{56b}$$

$$U_0 = \frac{R_0}{T_0}, \tag{56c}$$

where T_0 is the capilary time scale. As a consequence the dimensionless numbers become:

$$\mathbb{R}\text{e} = \mathbb{O}\text{h}^{-1}, \tag{57a}$$

$$\mathbb{F}\text{r} = \mathbb{E}\text{o}^{-1/2}, \tag{57b}$$

$$\mathbb{W}\text{e} = 1, \tag{57c}$$

where the Ohnesorge number ($\mathbb{O}\text{h}$) and the Eötvös number ($\mathbb{E}\text{o}$) are given by:

$$\mathbb{O}\text{h} = \frac{\nu_1}{\sqrt{\rho_1 R_0 \sigma}}, \tag{58a}$$

$$\mathbb{E}\text{o} = \frac{\rho_1 g R_0^2}{\sigma}. \tag{58b}$$

The Eötvös number ($\mathbb{E}\text{o}$) describes the relative importance of gravity and surface tension, and is also known as the Bond number ($\mathbb{B}\text{o}$).

The system is now characterized by 6 dimensionless quantities: $\Gamma_0, \mathbb{O}\text{h}, \mathbb{E}\text{o}, \mathbb{C}\text{n}, \rho_1/\rho_2$ and ν_1/ν_2. The experiment is conducted over a time period of $10.7 \times 10^{-3}\text{s}$, which corresponds to final time $T_{\text{end}} = 62.6867\,T_0$. We set $\Delta t_n = 0.002\,T_{\text{end}}$. The Cahn number is taken as $\mathbb{C}\text{n} = 0.64h$. The other dimensionless quantities

are given in Table 5.

ρ_1/ρ_2	ν_1/ν_2	$\mathbb{O}$h	$\mathbb{E}$o
1000	100	1.01	0.0022

Table 5: Parameters for the three-dimensional ligament contraction case.

In Figure 14 we qualitatively compare our computational results of the contracting liquid filament with the experimental data of Castrejon et al. [27]. We observe an overall good agreement between the computation and the experiment. In particular, the length of the liquid filament matches well. We see a slight deviation in the vertical position of the filament. This might be the consequence of a non-zero downwards velocity of the experiment at the initial time. Finally, we note that experimental results show that the filament does not break up (this is hard to detect in the last frame). In fact, Castrejon et al. [27] find that at this $\mathbb{O}$h number the filament never breaks up, even for very large aspect ratios Γ_0. Our computational results confirm this observation.

(a) $t = 0.0 \times 10^{-3}$s (num)　　(b) $t = 0.0 \times 10^{-3}$s (exp)　　(c) $t = 4.0 \times 10^{-3}$s (num)　　(d) $t = 4.0 \times 10^{-3}$s (exp)

(e) $t = 6.3 \times 10^{-3}$s (num)　　(f) $t = 6.3 \times 10^{-3}$s (exp)　　(g) $t = 10.7 \times 10^{-3}$s (num)　　(h) $t = 10.7 \times 10^{-3}$s (exp)
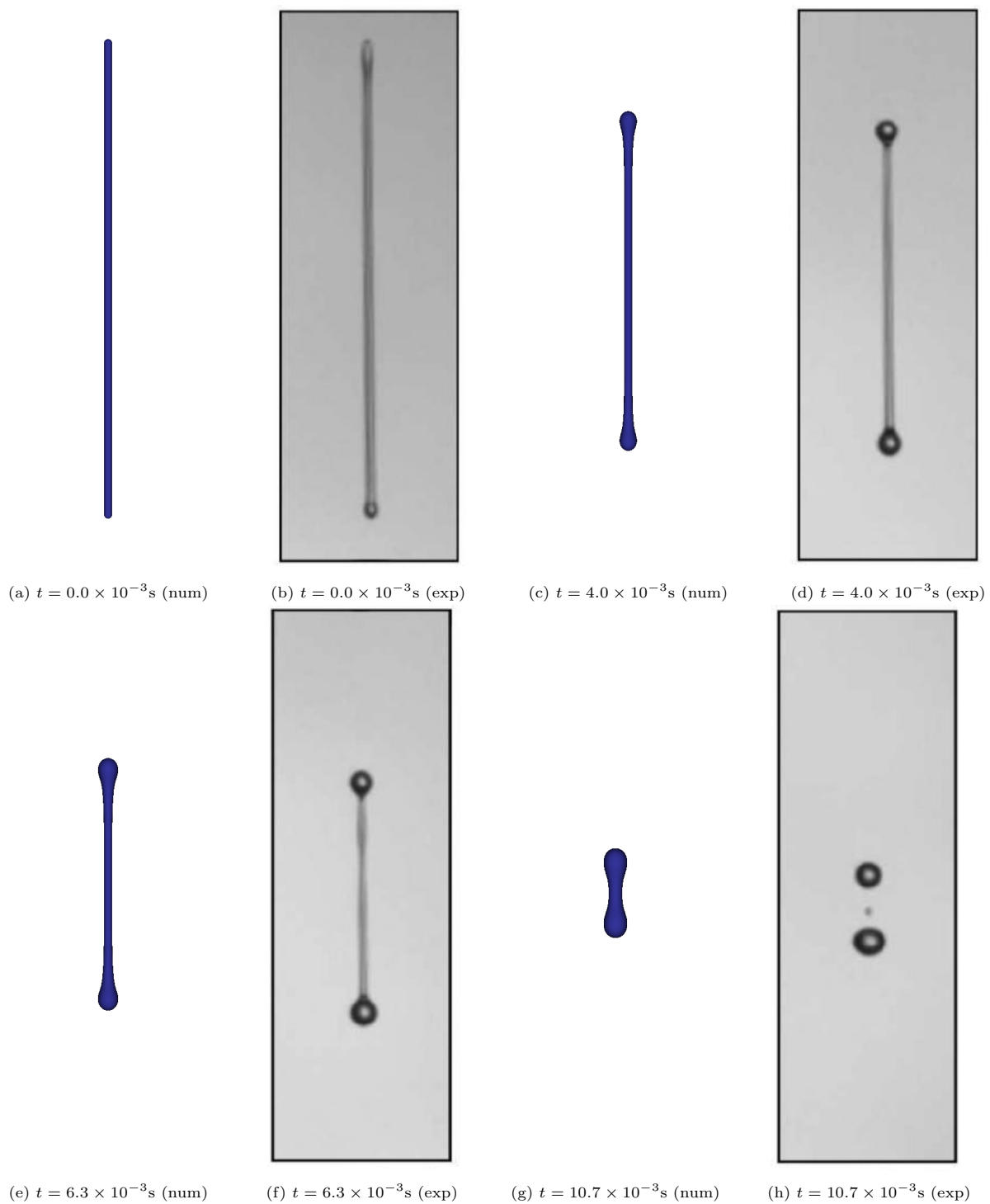
Figure 14: Ligament contraction problem. Shape of the ligament using the numerical simulation (num) experimental results (exp).

6. Conclusion and outlook

In this paper we have presented the consistent Navier-Stokes Cahn-Hilliard (NSCH) model with non-matching densities, alongside with a numerical methodology, and verification and validation studies. The NSCH model is a diffuse-interface energy-stable model that describes the motion of a mixture of fluids, and is derived from continuum mixture theory. The NSCH model is a single model, not a collection of models, that is invariant to the choice of fundamental variables. The mixture theory derivation naturally leads to a formulation in terms of the mass-averaged velocity. In order to circumvent the challenges of directly discretizing this NSCH formulation, we have adopted an equivalent formulation in terms of the divergence-free volume-averaged velocity. We have discretized this formulation using divergence-conforming isogeometric spaces. Finally, we have verified and validated the the methodology using two-dimensional test cases, and three-dimensional benchmark computations of rising bubbles and the contraction of a liquid filament. These three-dimensional computations compare well with experimental data. Concluding, we have proposed a NSCH computational framework that:

- uses the consistent NSCH model which naturally emerges from continuum mixture theory;

- employs a non-standard form of the NSCH model which properly accounts for the diffuse flux contribution in the momentum equation;

- uses a degenerate mobility;

- reduces in the single-fluid regime to the incompressible Navier-Stokes equations;

- uses a pointwise divergence-free velocity discretization in the entire computational domain;

- permits large density ratios;

- has a stable interface, and thus refrains from interface stabilization techniques;

- shows good agreement with experimental data.

We delineate some potential avenues for future research. First, regarding the mathematical analysis, establishing sharp interface asymptotics remains an important open problem. This sharp interface problem is invariant to the choice of fundamental variables in the NSCH model. Second, in regards to computation, the extension to high Reynolds number flow necessitates widely applicable and robust turbulence models. We anticipate that (energy-dissipative) variational multiscale stabilization mechanisms are well-suited for this purpose, e.g. by building onto [28, 29].

References

[1] P.C. Hohenberg and B.I. Halperin. Theory of dynamic critical phenomena. *Reviews of Modern Physics*, 49:435, 1977.

[2] M.E. Gurtin, D. Polignone, and J. Vinals. Two-phase binary fluids and immiscible fluids described by an order parameter. *Mathematical Models and Methods in Applied Sciences*, 6:815–831, 1996.

[3] J. Lowengrub and L. Truskinovsky. Quasi–incompressible cahn–hilliard fluids and topological transitions. *Proceedings of the Royal Society of London. Series A: Mathematical, Physical and Engineering Sciences*, 454:2617–2654, 1998.

[4] F. Boyer. A theoretical and numerical model for the study of incompressible mixture flows. *Computers & fluids*, 31:41–68, 2002.

[5] H. Ding, P.D.M. Spelt, and C. Shu. Diffuse interface model for incompressible two-phase flows with large density ratios. *Journal of Computational Physics*, 226:2078–2095, 2007.

[6] H. Abels, H. Garcke, and G. Grün. Thermodynamically consistent, frame indifferent diffuse interface models for incompressible two-phase flows with different densities. *Mathematical Models and Methods in Applied Sciences*, 22:1150013, 2012.

[7] J. Shen, X. Yang, and Q. Wang. Mass and volume conservation in phase field models for binary fluids. *Communications in Computational Physics*, 13:1045–1065, 2013.

[8] G.L. Aki, W. Dreyer, J. Giesselmann, and C. Kraus. A quasi-incompressible diffuse interface model with phase transition. *Mathematical Models and Methods in Applied Sciences*, 24:827–861, 2014.

[9] M. Shokrpour Roudbari, G. Şimşek, E.H. van Brummelen, and K.G. van der Zee. Diffuse-interface two-phase flow models with different densities: A new quasi-incompressible form and a linear energy-stable method. *Mathematical Models and Methods in Applied Sciences*, 28:733–770, 2018.

[10] M.F.P. ten Eikelder, K.G. van der Zee, I. Akkerman, and D. Schillinger. A unified framework for Navier–Stokes Cahn–Hilliard models with non-matching densities. *Mathematical Models and Methods in Applied Sciences*, 33:175–221, 2023.

[11] C. Truesdell and R. Toupin. The classical field theories. In *Principles of classical mechanics and field theory/Prinzipien der Klassischen Mechanik und Feldtheorie*, pages 226–858. Springer, 1960.

[12] C. Truesdell. Rational thermodynamics. Springer, 1984.

[13] M.F.P. ten Eikelder, K.G. van der Zee, and D. Schillinger. Thermodynamically consistent diffuse- interface mixture models of incompressible multicomponent fluid. *arXiv preprint arXiv:2302.09287*, 2023.

[14] S. Aland. Time integration for diffuse interface models for two-phase flow. *Journal of Computational Physics*, 262:58–71, 2014.

[15] P. Yue. Thermodynamically consistent phase-field modelling of contact angle hysteresis. *Journal of Fluid Mechanics*, 899:A15, 2020.

[16] S.R. Bhopalam, J. Bueno, and H. Gomez. Elasto-capillary fluid–structure interaction with compound droplets. *Computer Methods in Applied Mechanics and Engineering*, 400:115507, 2022.

[17] L.F.R. Espath, A.F. Sarmiento, B.O.N. Varga, and A.M.A. Cortes. Energy exchange analysis in droplet dynamics via the Navier–Stokes–Cahn–Hilliard model. *Journal of Fluid Mechanics*, 797:389–430, 2016.

[18] M.F.P. ten Eikelder and I. Akkerman. A novel diffuse-interface model and a fully-discrete maximum-principle-preserving energy-stable method for two-phase flow with surface tension and non-matching densities. *Computer Methods in Applied Mechanics and Engineering*, 379:113751, 2021.

[19] J.A. Evans and T.J.R. Hughes. Isogeometric divergence-conforming B-splines for the unsteady Navier–Stokes equations. *Journal of Computational Physics*, 241:141–167, 2013.

[20] S. Hysing, S. Turek, D. Kuzmin, N. Parolini, E. Burman, S. Ganesan, and L. Tobiska. Quantitative benchmark computations of two-dimensional bubble dynamics. *International Journal for Numerical Methods in Fluids*, 60:1259–1288, 2009.

[21] S. Aland and A. Voigt. Benchmark computations of diffuse interface models for two-dimensional bubble dynamics. *International Journal for Numerical Methods in Fluids*, 69:747–761, 2012.

[22] S. Balay, W.D. Gropp, L. McInnes, and B.F. Smith. Efficient management of parallelism in object oriented numerical software libraries. In E. Arge, A. M. Bruaset, and H. P. Langtangen, editors, *Modern Software Tools in Scientific Computing*, pages 163–202. Birkhäuser Press, 1997.

[23] J. Yan, S. Lin, Y. Bazilevs, and G.J. Wagner. Isogeometric analysis of multi-phase flows with surface tension and with application to dynamics of rising bubbles. *Computers & Fluids*, 179:777–789, 2019.

[24] D. Bhaga and M.E. Weber. Bubbles in viscous liquids: shapes, wakes and velocities. *Journal of fluid Mechanics*, 105:61–85, 1981.

[25] J. Hua, J.F. Stene, and P. Lin. Numerical simulation of 3D bubbles rising in viscous liquids using a front tracking method. *Journal of Computational Physics*, 227:3358–3382, 2008.

[26] L. Amaya-Bower and T. Lee. Single bubble rising dynamics for moderate reynolds number using lattice boltzmann method. *Computers & Fluids*, 39:1191–1207, 2010.

[27] A.A. Castrejón-Pita, J.R. Castrejón-Pita, and I.M. Hutchings. Breakup of liquid filaments. *Physical review letters*, 108:074506, 2012.

[28] M.F.P. ten Eikelder and I. Akkerman. Correct energy evolution of stabilized formulations: The relation between VMS, SUPG and GLS via dynamic orthogonal small-scales and isogeometric analysis. II: The incompressible Navier-Stokes equations. *Computer Methods in Applied Mechanics and Engineering*, 340:1135–1159, 2018.

[29] J.A. Evans, D. Kamensky, and Y. Bazilevs. Variational multiscale modeling with discretely divergence-free subscales. *Computers & Mathematics with Applications*, 2020.